RESEARCH ARTICLE

NANO · MICRO small
www.small-journal.com

Superwetting, Self-Sterilizing Cu/CuZn-ZnO Grating via Laser Engineering for Advanced Droplet Sensing

*Yexin Pan, Xupeng Lu, Ruohan Yu, Le Jing, Yang Xu, Wing Yan Poon, Haosong Zhong, Siyu Chen, Molong Duan, Yang Liu, and Mitch Guijun Li**

Controlling metal properties is essential for achieving functional applications, as metals show extreme tunability on surface energies, structural surface areas, and sterilization ability. Existing materials for respiratory droplet detection, critical for controlling infectious disease spread, often lack combined extreme wettability and intrinsic antimicrobial activity. Inspired by the photonic crystals of peacock feathers, a highly sensitive and self-sterilizing optical grating sensor is developed based on a core-shell nanostructured copper/copper-zinc and zinc oxide (Cu/CuZn-ZnO) composite (interconnected Cu or CuZn nanoparticles encapsulated by ZnO). A two-step laser-induced process controls the composite's properties, creating hierarchical, core-shell nanostructures and simultaneously tailoring surface energy and morphology for superhydrophilicity. This laser-engineered superwetting surface, combining increased surface area and low surface energy, amplifies aqueous droplet footprint diameter over fivefold, enabling picoliter-range electrical detection. The amounts and distribution of droplets can be analyzed using point-to-point optical Fourier translation analysis and classical statistics. The laser-generated ZnO and residual copper species provide inherent antimicrobial properties, achieving effective self-disinfection. This integrated superhydrophilicity and self-disinfection platform offers significant potential for advanced respiratory droplet analysis and public health monitoring.

1. Introduction

The Coronavirus disease 2019 (COVID-19) pandemic engendered profound global consequences, with more than 770 million cases and 7 million fatalities reported as of October 9, 2024.[1] This pandemic has significantly disrupted societal functions, particularly in production, trade, and communication, etc. Sufficient research has verified human respiratory droplets and aerosols as the primary modes of rapid COVID-19 transmission.[2,3] These two transmission vectors are all liquid fragmentation generated during breathing, coughing, and sneezing, which can be distinguished by the diameter of larger or less than 5 μm.[4] The droplets keep a reported size of up to 1000 μm with a maximum travel distance of 2 m, while the aerosols can travel tens of meters with a minimum diameter of 0.1 μm.[5–9] Virus mutations have further complicated the issue, with severe acute respiratory syndrome coronavirus 2 (SARS-CoV-2) persisting on contaminated surfaces for days.[10,11] Similar transmission mechanisms are implicated in other respiratory infections, such as Mycoplasma pneumonia, influenza, tuberculosis, and chickenpox, accentuating a persistent public health imperative.[12,13] Consequently, rapid detection of respiratory droplets and aerosols in public spaces is crucial for identifying high-incidence areas and implementing preventative measures.

Efforts to mitigate pathogen transmission, particularly during the COVID-19 pandemic, have spurred advancements in individual sensing systems, often integrated into masks to complement traditional diagnostics.[14–17] These wearable platforms leverage diverse transduction mechanisms, including pressure,[18] triboelectric effects,[19,20] novel material responses (e.g., hydrogels, ion gels, nanostructures),[21–23] and optical techniques,[24,25] for monitoring physiological indicators or detecting viral components. However, persistent challenges include user discomfort hindering compliance with prolonged mask usage, and critically, the inherent limitation of such personal devices in assessing broader environmental risks posed by infectious droplets and aerosols.[26,27] Although direct environmental monitoring of these transmission vectors is vital, the field remains comparatively underdeveloped in terms of readily deployable and

Y. Pan, X. Lu, R. Yu, L. Jing, Y. Xu, W. Y. Poon, H. Zhong, S. Chen, M. G. Li
Center for Smart Manufacturing
Division of Integrative Systems and Design
The Hong Kong University of Science and Technology
Clear Water Bay, Kowloon, Hong Kong SAR 999077, China
E-mail: mitchli@ust.hk

R. Yu
The Sanya Science and Education Innovation Park
Wuhan University of Technology
Sanya 572000, China

M. Duan
Center for Smart Manufacturing
Department of Mechanical and Aerospace Engineering
The Hong Kong University of Science and Technology
Clear Water Bay, Kowloon, Hong Kong SAR 999077, China

Y. Liu
Department of Applied Physics
The Hong Kong Polytechnic University
Hong Kong, Hong Kong SAR 999077, China

The ORCID identification number(s) for the author(s) of this article can be found under https://doi.org/10.1002/smll.202502976

DOI: 10.1002/smll.202502976

effective technologies. Current environmental surveillance often relies on aerosol collection followed by time-consuming laboratory analysis.[28] While in situ platforms employing biosensors[29,30] or microfluidics[7] offer faster detection of specific targets, they face limitations in broad applicability or sensitivity. Furthermore, commercial particle counters, though widely used for aerosol research, often require enhanced signal sensitivity to effectively characterize potentially hazardous bioaerosols.[31,32] These multifaceted shortcomings in both personal and environmental surveillance highlight a critical gap and underscore the inadequacy of existing tools to comprehensively address ambient pathogen threats.

Consequently, there is an exigent demand for advanced materials systems capable of dynamically detecting, controlling, and mitigating the risks associated with infectious aerosolized and droplet-borne pathogens. Specifically, surfaces engineered to possess concurrent anti-droplet (hydrophilic control), droplet-sensing, and antimicrobial functionalities represent a compelling paradigm for minimizing disease propagation vectors. Prior investigations have indeed addressed separate facets of this complex problem. The creation of superhydrophilic surfaces, through techniques such as plasma treatment, wet chemical treatment, and deposition of hydrophilic polymers, has been explored to precisely control surface wettability for various applications.[33–35] However, laser-based fabrication methods offer a unique combination of advantages over many traditional approaches, including precise spatial and morphological control critical for micro- and nano-structures, versatility in processing diverse materials including metals and oxides, direct maskless pattern generation, rapid processing, and scalability.[36–38] These attributes make laser techniques particularly well-suited for creating complex, micro-structured functional surfaces like the grating investigated here. Separately, droplet sensing technologies have advanced rapidly, employing diverse principles such as capacitance/resistance changes,[39,40] triboelectric effects,[19,20] and optical techniques.[41] While achieving sensitivity, many existing sensors struggle with integrating robust surface wettability control (often favoring hydrophobicity) and lack intrinsic mechanisms for pathogen inactivation. Furthermore, the development of antimicrobial surfaces, frequently utilizing materials like copper or zinc oxide known for disrupting microbial membranes, has progressed significantly, including laser-based fabrication routes.[42–45] However, a critical deficiency persists, as these advancements have largely progressed independently. Laser-fabricated surfaces are commonly engineered to optimize either specific wettability characteristics or antimicrobial efficacy, but infrequently incorporate sensing capabilities. Conversely, dedicated sensing platforms typically lack inherent antimicrobial functionalities and the requisite surface wettability conducive to efficient droplet capture and analysis relevant to respiratory transmission scenarios.

Inspired by the vibrant feathers of peacocks, optical methods have demonstrated the feasibility of exploring the small-scale structure via macroscopic visible phenomena.[46] The comb-shaped natural photonic crystal structure guides our initial design of the optical diffraction components. Combining optical sensing systems with superhydrophilic component interfaces offers a potential solution to the challenge of optical signal amplification, as the surface wettability promotes rapid droplet spreading.[36–38] Based on the diffraction pattern observed from a peacock feather (**Figure 1a**), we fabricated the bio-inspired copper/copper-zinc and zinc oxide (Cu/CuZn-ZnO) grating by a laser-induced method, resulting in a 3D network of ZnO-encapsulated Cu or CuZn core-shell nanoparticles. This nanostructure exhibits excellent hydrophilicity and antibacterial properties. The enhanced surface wettability facilitates the rapid spreading and effective magnification of minute airborne droplets, leading to two distinct and measurable phenomena. First, droplet contact bridges the micro-scale grating lines, resulting in a quantifiable decrease in electrical resistance, as illustrated in Figure 1b, enabling rapid and sensitive droplet detection. Second, droplet impingement induces distinct alterations in the observed diffraction patterns (Figure 1c). Dry regions maintain a well-defined, 1D diffraction pattern, whereas droplet-covered areas display a significantly diminished or absent pattern, indicative of the disruption of the periodic grating structure by the liquid. This differential diffraction response allows for precise spatial localization of droplet deposition, which can be further quantified through point-to-point optical Fourier transform analysis in conjunction with classical statistical methods. Beyond its sensing capabilities, the grating demonstrates exceptional bactericidal performance (Figure 1d), attributed to the synergistic effects of the laser-induced nanostructured morphology and the inherent antimicrobial properties of the constituent materials. The sensor's trifecta of electrical and optical detection capabilities, combined with potent antibacterial activity, represents a significant advancement, positioning it as a valuable tool for applications spanning environmental monitoring to public health.

2. Results and Discussion

This study introduces a novel approach to grating fabrication, diverging from traditional optical gratings by engineering a Cu/CuZn-ZnO grating that exhibits superhydrophilic, antibacterial, and optical slit properties. The grating structure was realized using a two-step laser-based process, illustrated in **Figure 2a**. Initially, laser-induced backward transfer (LIBT) was employed to deposit CuZn alloy from a bulk sheet onto a glass substrate. Subsequently, laser direct writing (LDW) was utilized for precise ablation of the excess material, resulting in the desired grating geometry. A representative optical image of the fabricated grating is provided in Figure S1 (Supporting Information). Conductive copper tape was applied to both lateral edges of the grating to facilitate electrical conductivity measurements. The optical image clearly demonstrates the electrical isolation between the left and right sides of the grating. Moreover, a non-uniform grating line density is evident, characterized by a higher line density in the central region and a lower density towards the periphery. Optical microscopy displays that the grating's central region exhibits a line spacing of approximately 65 µm and a linewidth of 60 µm, as shown in Figure 2b. Contact angle measurements, presented in Figure 2c, confirm the superhydrophilic nature of the fabricated grating, exhibiting a remarkably low contact angle of 2.3 °. This is significantly lower than the contact angles of the pristine glass substrate (35.1 °, Figure S2, Supporting Information) and the pristine brass (103.0 °, Figure S3, Supporting Information), underscoring the substantial enhancement in hydrophilicity achieved through the laser transfer process. Based on the

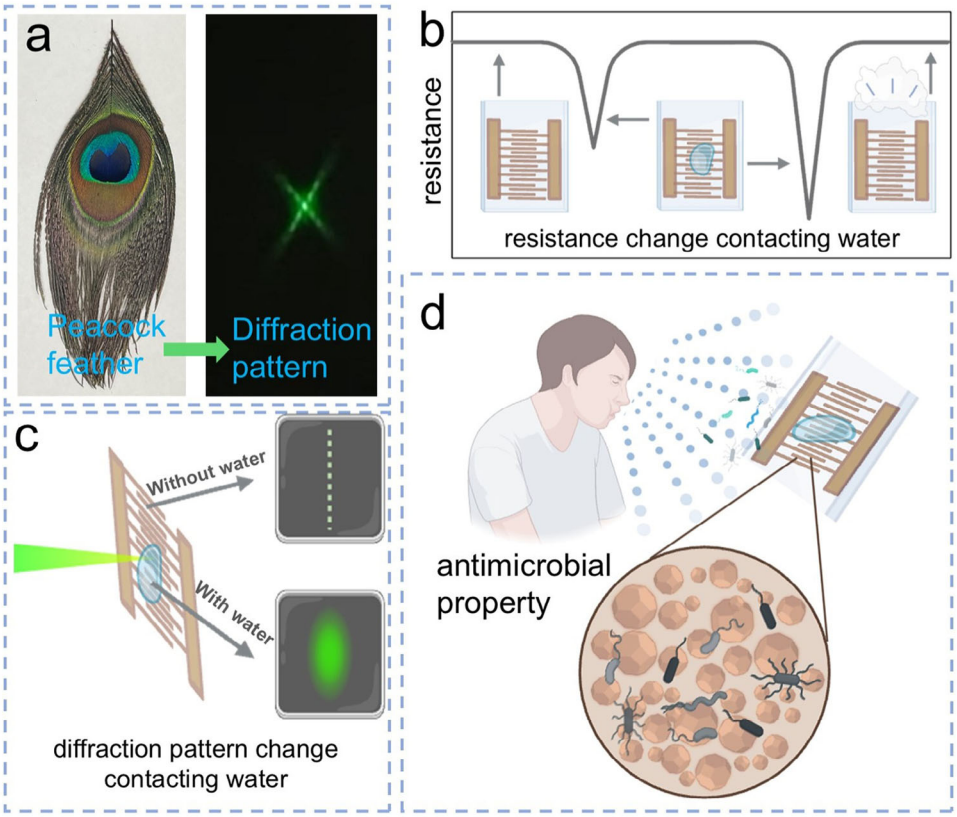

Figure 1. a) Optical image of peacock feather and corresponding diffraction pattern; b) electrical resistance sensing of droplet collection on a fabricated grating; c) comparative analysis of diffraction patterns from a grating in the absence and presence of water droplets; d) demonstration of a fabricated grating for droplet collection with antibacterial properties.

measured contact angle of the fabricated grating, calculations illustrate that the length of D2 is more than five times that of D1. Consequently, upon contact with a water droplet, the hydrophilic grating significantly increases its spreading radius, rendering it highly effective for detecting minute liquid volumes.

Figure 2d shows the X-ray diffraction (XRD) results of the brass before and after laser processing. The XRD pattern of the raw brass reveals characteristic peaks corresponding to ZnO and CuZn alloy ($Cu_{0.7}Zn_{0.3}$ and $Cu_{0.5}Zn_{0.5}$). After laser processing, a new distinct peak emerges at 43.5 °, which is attributed to the presence of elemental Cu. At the same time, no significant changes occur on other peaks, which proves that the laser processing can reduce part of CuZn alloy to Cu. Figure 2e shows the scanning electron microscopy (SEM) image of the CuZn alloy laser-induced backward transferred onto a glass substrate. The image reveals closely packed nanoparticles forming a continuous layer that fully covers the substrate, resulting in excellent conductivity with a resistance of only tens of ohms. Figures S4 and S5 (Supporting Information) present the SEM images and corresponding elemental mapping of both pristine brass powder (obtained through polishing and grinding) and Cu/CuZn-ZnO grating samples, indicating the presence of Cu, Zn, and O throughout the samples. Comparative map sum spectral analysis (Figure S6, Supporting Information) of pristine brass and a laser-patterned brass grating reveals a substantial elevation in oxygen concentration within the laser-processed sample. The elevated oxygen content is explicable considering the high-temperature nature of the laser transfer process conducted in ambient atmospheric conditions, which facilitates the occurrence of oxidation reactions during material processing. Figure S7 (Supporting Information) shows the nitrogen adsorption-desorption isotherms, indicating the average pore diameter and specific surface area of Cu/CuZn-ZnO is 28.9 nm and 8.33 m^2g^{-1}, respectively.

Figure 2f displays the high-angle annular dark field (HAADF) scanning transmission electron microscopy (STEM) image and corresponding energy dispersive X-ray spectroscopy (EDX) elemental mapping, revealing a network structure comprised of interconnected nanoparticles. The EDX mapping confirms the presence of Cu, Zn, and O throughout the entire structure. However, a non-uniform elemental distribution is observed, particularly evident in areas 1 and 2, as highlighted in the EDX analysis (Figure 2g). Area 1 exhibits a significantly higher Cu content compared to Zn, whereas area 2 shows a more balanced distribution of Cu and Zn, suggesting the coexistence of elemental Cu and CuZn alloy phases. Higher-magnification STEM imaging and corresponding elemental mapping (Figure S8, Supporting Information) further corroborate the non-uniform distribution of Cu and Zn, supporting the presence of both elemental Cu and ZnO within the structure. The nanostructure was further studied by atomic resolution HAADF-STEM and corresponding EDX mapping, as displayed in Figure 2h. A clear contrast difference is observed between the inner and outer regions of the

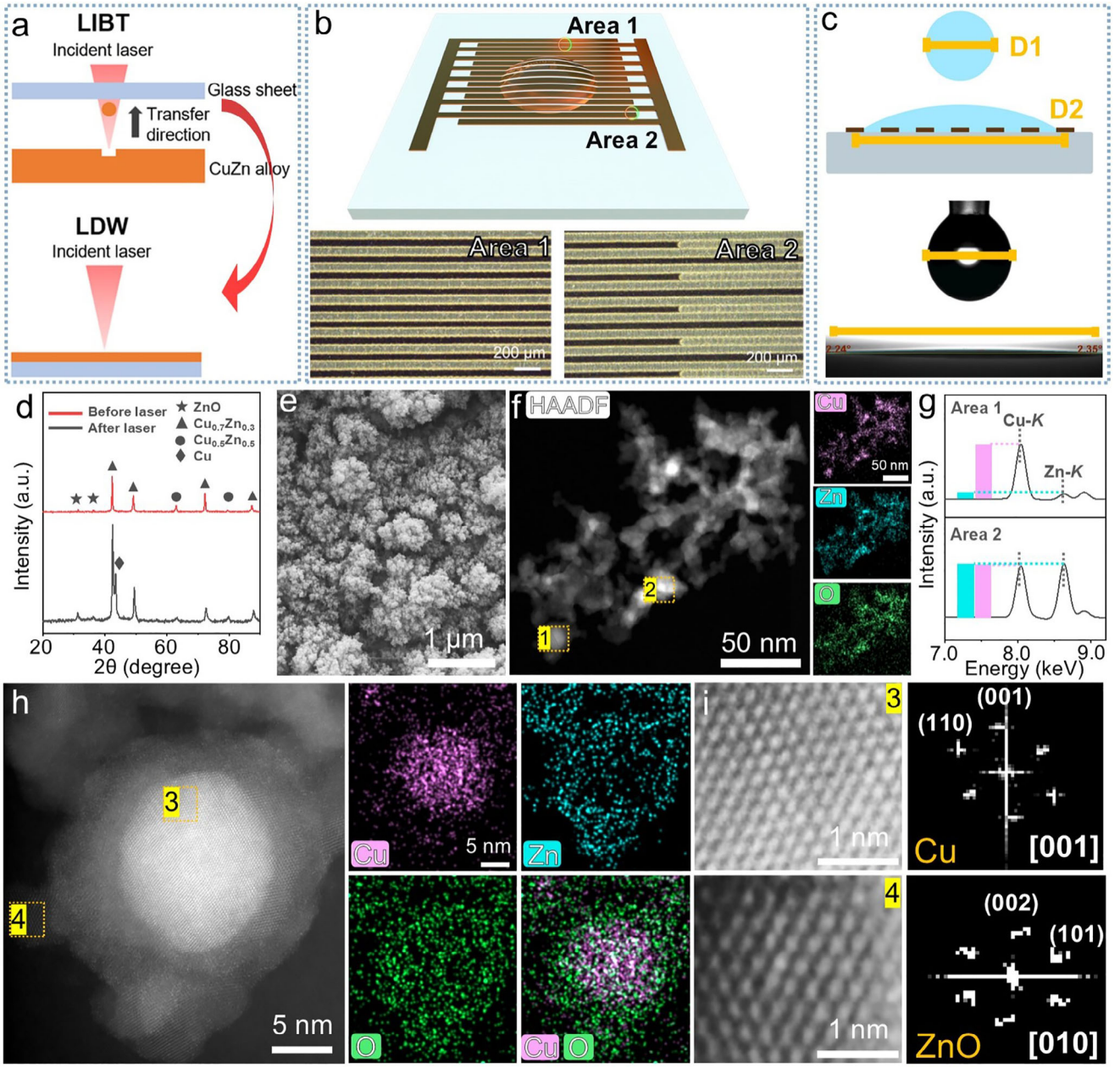

Figure 2. a) Fabrication process of the Cu/CuZn-ZnO grating; b) illustration when the Cu/CuZn-ZnO grating contacting with water and optical microscopy images of the grating's central region and and edge region; c) illustration of droplet before and after contact with the Cu/CuZn-ZnO grating and contact angle test for the Cu/CuZn-ZnO grating; d) XRD patterns of the Cu/CuZn-ZnO grating and raw brass; e) SEM image, f) HAADF STEM and corresponding EDX mapping images of Cu/CuZn-ZnO grating; g) EDX spectra from area 1 and 2 in (f); h) high-resolution HAADF STEM image and corresponding EDX mapping images of Cu/CuZn-ZnO grating; i) magnified HAADF image of area 3 and area 4 in (h) and corresponding FFT.

nanoparticles, with the inner core exhibiting higher contrast. The EDX mapping reveals a heterogeneous distribution of Cu, Zn, and O. Notably, the inner core is enriched with Cu, indicative of elemental Cu formation, which explains the higher contrast observed. Conversely, the distribution of Zn shows a spatial correlation with that of O, suggesting the formation of ZnO, thus resulting in a lower contrast in the outer region. Figure 2i illustrates the fast Fourier transform (FFT) images of area 3 (inner part) and area 4 (outer part) from the STEM image (Figure 2h), indicating a metal Cu [001] and a ZnO [010] zone axis in the inner and outer regions, respectively.

The 3D tomographic reconstruction technique was employed to investigate the microstructural features of the grating in greater detail. A dataset of 72 HAADF-STEM images was acquired every 2 degrees for reconstruction, as shown in **Figure** 3a and Video S1 (Supporting Information). The reconstructed model displayed in Figure 3b, aligns with the image framed in red within Figure 3a, which was captured at 70 °. Along the length,

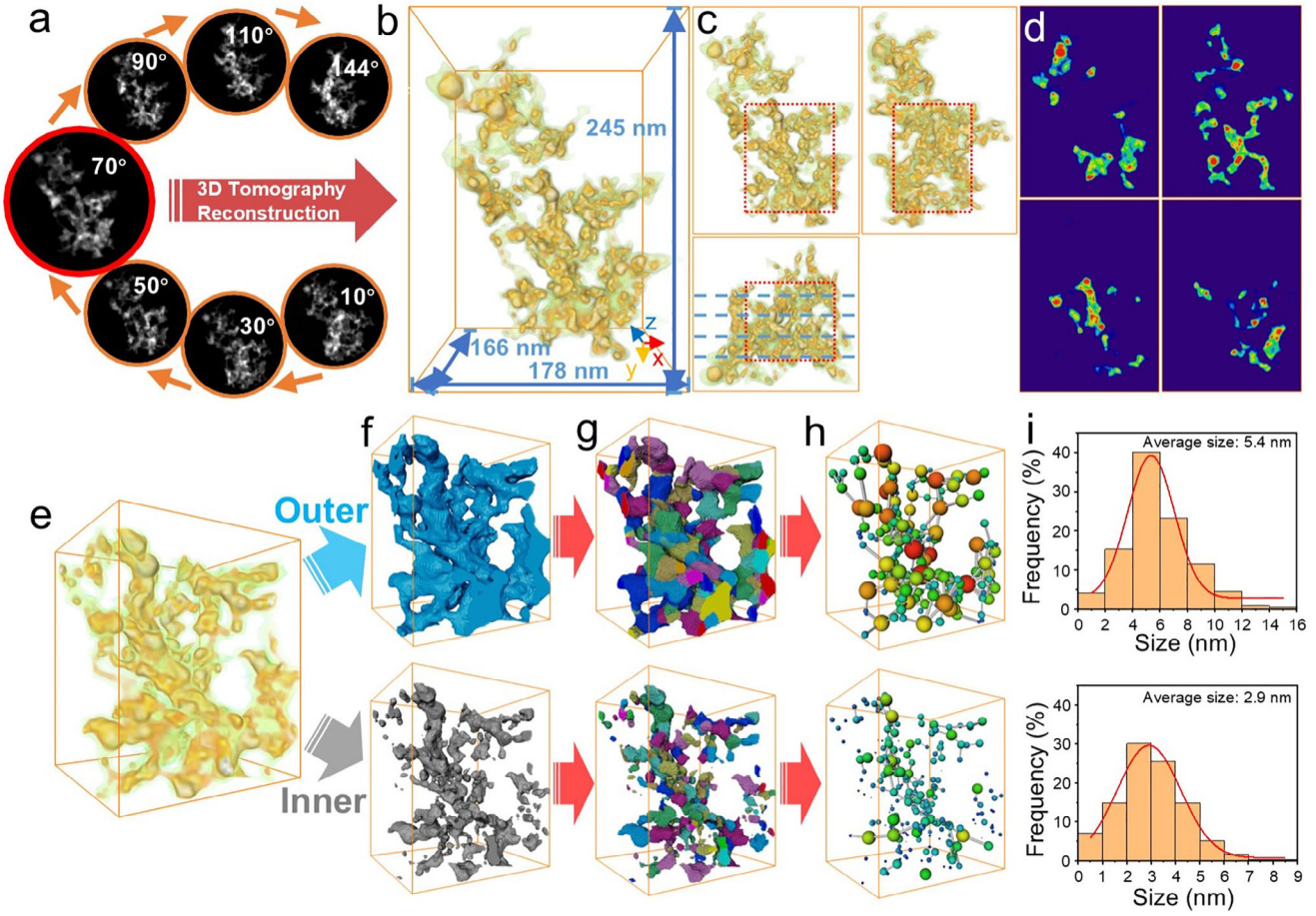

Figure 3. a) Representative HAADF-STEM images at different rotation angles; b) reconstructed Cu/CuZn-ZnO grating sample model; c) three view drawing of the reconstructed model; d) representative orthoslices; e) extracted volume form the red dash line in (c); f) volume segmentation by contrast; g) volume separation; h) generated network model; i) size distribution of the inner conductive part and the whole structure.

width and height, this model's bounding box extends 178 nm (x), 166 nm (z), and 245 nm (y), respectively. In the HAADF images, the green volume and yellow volume represent low and high contrast, respectively. Consequently, the green volume is attributed to metal oxides, while the yellow signifies Cu and CuZn alloy regions. It is observed that the inner part of metal and alloy is mostly continuous and is encapsulated by the outer part of the metal oxide, which is also revealed by the three-view drawing (Figure 3c) and ortho slices (Figure 3d). To gain deeper insight into the internal structural connectivity, a sub-region, delineated by the red dashed line in Figure 3c, was extracted from the reconstructed model and is presented in detail in Figure 3e. Variations in atomic number and density, discernible in the HAADF-STEM images, enabled the segmentation of the inner core region (composed of Cu and CuZn alloy) from the entire structure, including the outer ZnO layer, as illustrated in Figure 3f. A watershed algorithm applied via the "Separate Objects" module distinguished and color-coded topologically distinct inner conductive part and the whole structure within the sub-volume (Figure 3g). Volume-equivalent sphere representations (Figure 3h) further visualized these components, with warmer and cooler colors indicating larger interconnected conductive structures and smaller isolated part respectively, further highlighting the continuity of the inner conductive part. The size analysis presented in Figure 3i determined that the average radius of the inner conductive domain is 2.9 nm, compared to 5.4 nm for the outer domain.

The resistance of the Cu/CuZn-ZnO grating was measured under three conditions: (**Figure** 4a) as-fabricated Cu/CuZn-ZnO grating exposed to ambient air, (Figure 4b) Cu/CuZn-ZnO grating with a droplet of deionized water, and (Figure 4c) Cu/CuZn-ZnO grating with a droplet of electrolyte (0.1 M phosphate buffered saline, PBS). Figure 4d illustrates the change in resistance of the grating after adding a 0.1 µL water droplet. Upon contact, the resistance decreases dramatically due to the hydrophilic nature of the grating surface. The water droplet spreads rapidly, effectively bridging the gap between the two electrodes and leading to a sharp drop in resistance. However, the limited volume of water, coupled with its increased surface area, results in rapid evaporation. Consequently, the resistance reverts to its initial value concomitant with the complete evaporation of the water droplet. Quantitatively, the addition of a 0.1 µL water droplet results in a transient resistance reduction to approximately 18% of its original value. In contrast, a comparative analysis using a commercial humidity sensor under the same conditions showed that its resistance remained above

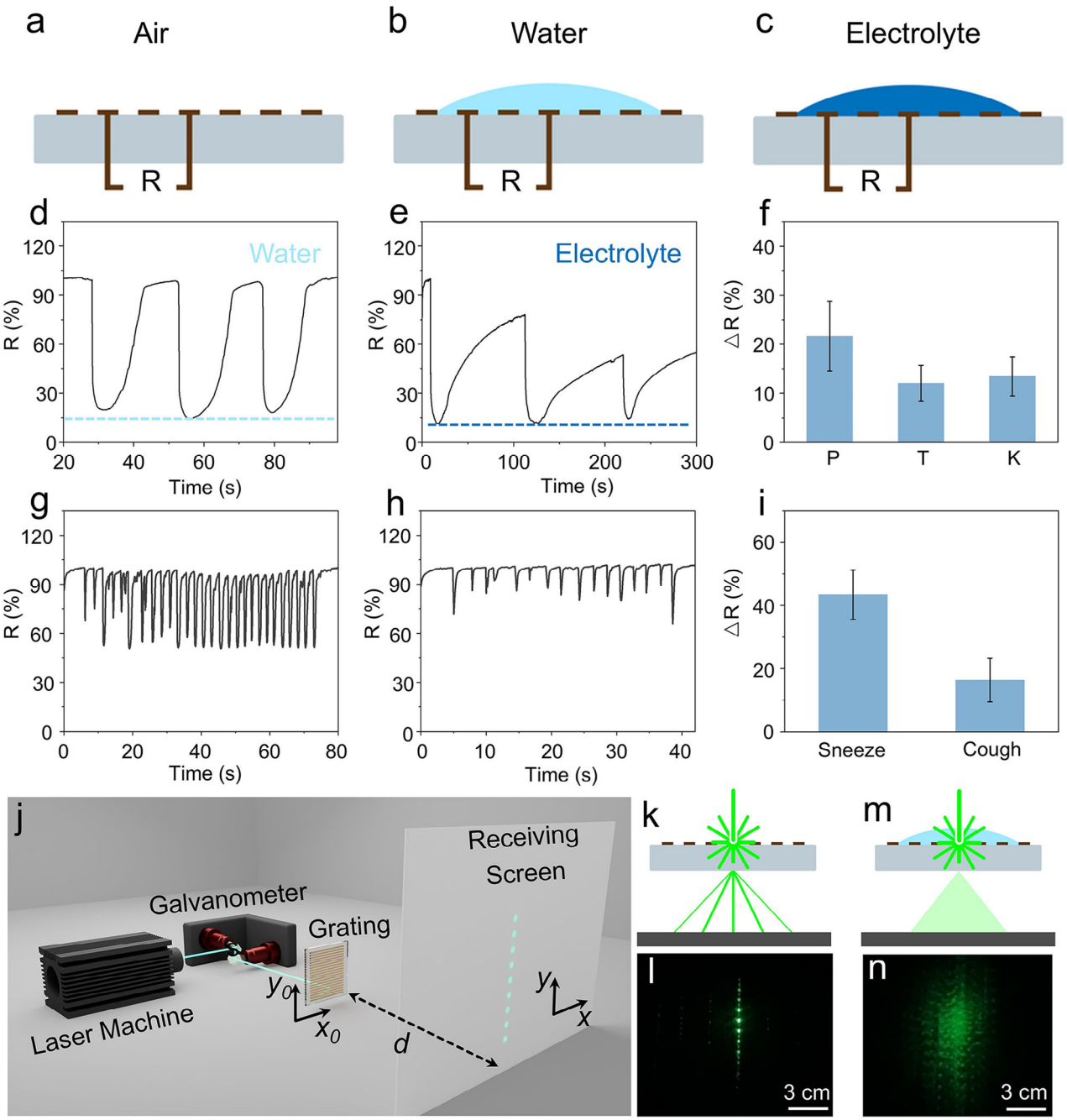

Figure 4. Resistance of the Cu/CuZn-ZnO grating was measured under three conditions: a) exposed to air; b) contact with deionized water; c) contact with electrolyte. Resistance change of the Cu/CuZn-ZnO grating after series of d) 0.1 µL water droplet addition and e) 0.1 µL electrolyte droplet addition; f) resistance change when uttering the letters "P", "T", and "K" while facing the Cu/CuZn-ZnO grating; resistance response of the Cu/CuZn-ZnO grating to g) sneezing and h) coughing; i) statistical analysis of the resistance decrease when sneezing and coughing to the Cu/CuZn-ZnO grating; j) illustration of grating diffraction system; k) illustration of the grating diffraction without water contact and l) corresponding real diffraction pattern; m) illustration of the grating diffraction with water contact and n) corresponding real diffraction pattern.

90% of its original value and a much longer recovery time of approximately 5 min as presented in Figure S9 (Supporting Information). This highlights the superior sensitivity and rapid response dynamics of Cu/CuZn-ZnO sensor for discrete micro-droplet detection compared to the conventional humidity sensor.

On the other hand, the resistance response of the grating to the addition of a 0.1 µL PBS droplet exhibits a fundamentally different behavior, as demonstrated in Figure 4e. The initial PBS droplet induces the most pronounced resistance change, reducing it to approximately 12% of its original value. As the droplet evaporates, the resistance gradually increases but does not fully

recover to its initial value. This irreversible change likely stems from the residual inorganic salt in PBS remaining on the grating surface. These salt residues likely form a persistent, albeit higher resistance, conductive layer or bridge conductive features, effectively altering the baseline resistance of the sensor. Subsequent additions of 0.1 µL PBS droplets result in progressively smaller resistance reductions, with the second and third droplets yielding approximately 66% and 39% reductions, respectively. This observation implies a potential saturation effect or a cumulative baseline shift caused by progressive salt accumulation. From an analytical standpoint, this highlights a potential challenge for sensing electrolyte-rich biological fluids: the sensor exhibits memory effects and baseline drift due to non-volatile residues in the test conditions. However, it is important to note the inherent stability of the sensor material itself when exposed to PBS. First, the functional stability was investigated by comparing the sensor's resistance response to 0.1 M PBS measured on the 1st day and the 2nd day. As shown in Figure S10 (Supporting Information), the response profiles exhibited strong similarity across the two days, indicating reproducible performance characteristics under consistent conditions. Second, SEM was employed to assess morphological changes following PBS exposure. Micrographs of the Cu/CuZn-ZnO composite surface acquired before and after the PBS detection process (Figure S11, Supporting Information) demonstrate no significant changes to the material's microstructure, confirming its morphological stability during testing.

However, it is crucial to consider the significant scale difference: typical respiratory droplets possess volumes in the picoliter to femtoliter range, orders of magnitude smaller than the 0.1 µL droplets used in this experiment. Consequently, the mass of salt residue deposited by a single, realistic respiratory droplet would be minuscule. This suggests that while electrolyte accumulation is a factor, its impact on the sensor's baseline resistance resulting from individual, sparse droplet events in a real-world scenario might be negligible or would only manifest after prolonged exposure over a very extended period. To confirm the consistency and reliability of our sensor's performance, we assessed the reproducibility across multiple samples. We fabricated and tested six independent Cu/CuZn-ZnO grating sensors' resistance changes for a series of 0.1 µL water contact and 0.1 µL PBS contact, as shown in Figure S12 (Supporting Information). It is observed that the response profiles (magnitude of resistance change and temporal dynamics) are highly consistent across the three distinct samples for both water and PBS droplets.

The resistance response of the grating to human speech was also investigated. Articulation of the plosive consonants "P", "T", and "K" in proximity to the Cu/CuZn-ZnO grating resulted in transient resistance decreases of 22%, 12%, and 13%, respectively, as shown in Figure 4f. This response is attributed to the impaction of micro-droplets expelled during speech onto the Cu/CuZn-ZnO grating surface. Due to the ultra-hydrophilic nature of the grating, it exhibits an exceptional sensitivity to droplets, where even minute droplets can be significantly amplified, resulting in the bridging of the interdigitated lines of the grating. This bridging phenomenon subsequently induces a measurable decrease in electrical resistance. We further investigated the resistance response of the grating to sneezing and coughing at a distance of 10 cm. As depicted in Figure 4g,h, both actions elicited a transient decrease in resistance. Statistical analysis of the resistance drops revealed that sneezing resulted in a reduction of approximately 43%, while coughing led to a reduction of approximately 16%, as summarized in Figure 4i. These results indicate that sneezing induces the most significant rate of change in electrical resistance. This observation is rationalized by the significantly larger volume and higher velocity of droplets expelled during a sneeze compared to coughing, leading to a greater probability of droplet-induced line bridging within the grating and, consequently, a more pronounced alteration in electrical resistance. The response of the commercial humidity sensor to sneezing was also evaluated, yielding a minimal resistance reduction of just 1%, as shown in Figure S13 (Supporting Information). The Cu/CuZn-ZnO grating sensor's performance stability was evaluated over 15 days using exposure to droplets from sneezes under ambient conditions. Figure S14 (Supporting Information) displays that the sensor reliably generated relative resistance changes between 40–50% for these events, suggesting the sensing materials maintain responsiveness under repeated, realistic operational conditions.

The optical diffraction system employed in this study is schematically illustrated in Figure 4j, where a laser beam passing through a grating generates alternating bright and dark diffraction fringes. The system design is guided by the following principle. Combining the Fresnel-Kirchhoff diffraction formula and the Taylor expansion formula, the Fresnel integral formula explaining optical diffraction can be defined as follows:

$$S(x,y)=\frac{e^{ikd}}{i\lambda d}\iint_{-\infty}^{\infty}S_1(x_1,y_1)\exp\{\frac{ik}{2d}[(x-x_1)^2+(y-y_1)^2]\}dx_1dy_1 \quad (1)$$

$$l\approx d+\frac{(x-x_1)^2+(y-y_1)^2}{2d}\quad\left(\text{if}\quad d\gg\sqrt[3]{\frac{[(x-x_1)^2+(y-y_1)^2]}{4\lambda}}\right) \quad (2)$$

Where Equation (2) serves as the approximate condition for establishing Equation (1). (x, y) and (x_1, y_1) are the coordinates of points on the receiving screen and the diffraction screen. $S(x, y)$ and $S_1(x_1, y_1)$ represent the optical wavefunctions of these points. l and d are the distance between two points $(x, y)\&(x_1, y_1)$ and two screens. λ and $k=\frac{2\pi}{\lambda}$ represent the optical wavelength and the angular wavenumber, respectively. By further expanding Equation (2), the criterion equation for Fraunhofer diffraction can be obtained:

$$l\approx d-\frac{x_1x+y_1y}{d}+\frac{x^2+y^2}{2d}\quad\left(\text{if}\quad k\frac{(x_1^2+y_1^2)_{max}}{2d}\ll\pi\quad i.e.,\quad d\gg\frac{(x_1^2+y_1^2)_{max}}{\lambda}\right) \quad (3)$$

According to Equation (3), unlike small-scale holes, the receiving screen has no diffraction phenomenon from optical slits in the Y-direction. Regarding the optical grating proposed in this work, the average width of the optical slits is 60 µm. The utilized portable light source generates a laser beam with a wavelength of 532 nm and a spot radius of 1.312 mm (Figure S15, Supporting Information). Therefore, the criterion for satisfying Fraunhofer diffraction is $d\gg 0.423$ mm, indicating that the entire system has been significantly simplified without any necessary lenses to reduce the imaging distance and to meet Fraunhofer diffraction requirements. The experimental results align with the theoretical

predictions. As depicted in Figure 4k,l, a 1D point array is formed when a laser beam illuminates our grating. When the grating captures a droplet, water modifies the optical path difference in the infiltration area, leading to the disruption of the grating structure and the blurriness of the diffraction spot shown in Figures 4m and 4n. The diffraction pattern dynamic procedure is recorded in Video S2 (Supporting Information), indicating that the diffraction pattern undergoes a significant change when the laser beam transitions from a droplet-free region to a droplet-contained region. By analyzing the laser diffraction results, it becomes feasible to precisely determine the presence of liquid droplets within the illuminated region of the light spot. Furthermore, the superhydrophilic property enables droplets to disperse uniformly across the grating's surface, significantly broadening the scope of this effect. Thus, as the laser beam scans the grating sensor via two galvanometers, all the encountered droplets will be quickly pinpointed the location point by point. Through the enumeration of droplet presence at individual scanning points, we can estimate the area of the grating infiltrated by droplets with classical probability theory, facilitating the evaluation of the droplet quantity in the tested environment.

The antibacterial efficacy of the fabricated grating was assessed towards Staphylococcus aureus (S. aureus) and Escherichia coli (E. coli), as shown in **Figure 5**. Bacterial suspensions were deposited onto both the grating and the pristine brass sheet, followed by contact for varying durations, and then the bacteria were washed out for culture, as shown in Figure 5a. Figure 5b displays that the number of colonies on the grating decreases significantly with increasing contact time for both bacterial strains. Notably, after 2 min, virtually no colonies were observed on the grating, highlighting its robust antibacterial activity. In contrast, a substantial number of bacterial colonies persisted on the pristine brass surface even after 3 min of contact time, indicating a significant enhancement in antibacterial performance following the laser transfer process. The number of viable bacteria remaining on the grating and the pristine brass surface after different contact times was quantified and presented in Figure 5c,d. Remarkably, the grating exhibits exceptional bactericidal activity, eliminating over 99% of bacteria within a mere 2 min. These results underscore the superior antibacterial properties of the laser-fabricated grating.

The enhanced antibacterial efficacy may be attributed to several primary aspects. First, the LIBT induces a morphological transformation of the CuZn alloy from a bulk structure to a nanostructured morphology with particle sizes in the range of nanometers. Nanoparticles exhibit a higher surface area compared to their bulk counterparts. This implies that, for an equivalent mass, nanoparticles possess a greater surface area available for interaction with bacterial cells. Furthermore, the reduced size of nanoparticles leads to a higher proportion of surface atoms, potentially leading to increased reactivity and enhanced release of metal ions, which are known to be cytotoxic to bacteria.[47] Second, both copper and zinc oxide are well-documented antimicrobial agents. Literature extensively reports that the antibacterial mechanisms of nano-copper can involve factors such as copper ion release and the potential generation of reactive oxygen species (ROS), which can lead to oxidative damage of bacterial membranes and deoxyribonucleic acid (DNA).[48] Similarly, ZnO's antimicrobial activity is also widely attributed in the literature to multiple mechanisms, including the release of Zn^{2+} ions and the generation of ROS.[49] Additionally, beyond the individual actions of these components, some studies suggest potential synergistic interactions between copper and zinc oxide systems, leading to enhanced copper ion release compared to copper alone and potentially greater ROS generation than observed for ZnO alone under specific conditions.[50] Therefore, it is plausible that the potent bactericidal effect of our composite surface arises from a combination of these factors: the high surface area and reactivity conferred by the nanostructure, coupled with the established antimicrobial properties associated with both copper and zinc species. While the specific contributions and potential synergistic interplay of mechanisms like ion release and ROS generation within the unique laser-synthesized composite were not directly quantified in this study, the presence of these known antimicrobial components in a nanostructured form provides a strong basis for the observed enhanced antibacterial efficacy.

Given the prevalence of respiratory illnesses induced by imperceptible airborne aerosols, monitoring their concentration is paramount for assessing individual exposure risks to respiratory pathogens. Our novel laser-fabricated grating sample enables dual-mode sensing, facilitating both global and localized (pixelized) in situ measurement of respiratory droplet aerosol. In a large area of glass sensors, the average risk of acute respiratory disease and infectious risk of each person can be independently evaluated. In a modern mechanically ventilated medical environment, respiratory aerosol can be transmitted via multiple ways, such as central air-conditioning systems and even oxygen delivery systems. The complexity of such modern systems makes backtracking the infection chain hard. With our laser-transferred Cu/CuZn-ZnO grating droplet and aerosol detection technique, aerosol sensors can be deployed in multiple locations of the mechanical air ventilation devices to prevent the risk of cross-infection when these systems malfunction. This approach leverages a sensory fusion technology that integrates optical and electrical sensing modalities, thereby conferring superior sensitivity and reliability even when implemented in otherwise inaccessible air-handling units. In contrast to conventional chemical-based droplet sensing methods, our solution offers the potential for real-time, dynamic responsiveness to fluctuating environmental conditions. Furthermore, the high-throughput nature of our laser fabrication process enables the production of large-area glass substrates integrated with these droplet sensors, thus ensuring comprehensive droplet detection across expansive indoor spaces. By equipping all indoor air-handling units with these droplet-sensing devices, it becomes feasible to dynamically regulate the operational intensity of air purification systems, thereby optimizing power consumption while simultaneously minimizing the risk of cross-infection via effective aerosol removal.

3. Conclusion

This study presents a facile fabrication method for a Cu/CuZn-ZnO grating employing a combined LIBT and LDW process. This process generates hierarchical, core-shell nanostructures, comprising an interconnected network of metallic Cu and CuZn alloy nanoparticles encapsulated by a ZnO shell. The resulting grating exhibits dual functionality, demonstrating both superhydrophilic and antibacterial properties, which were

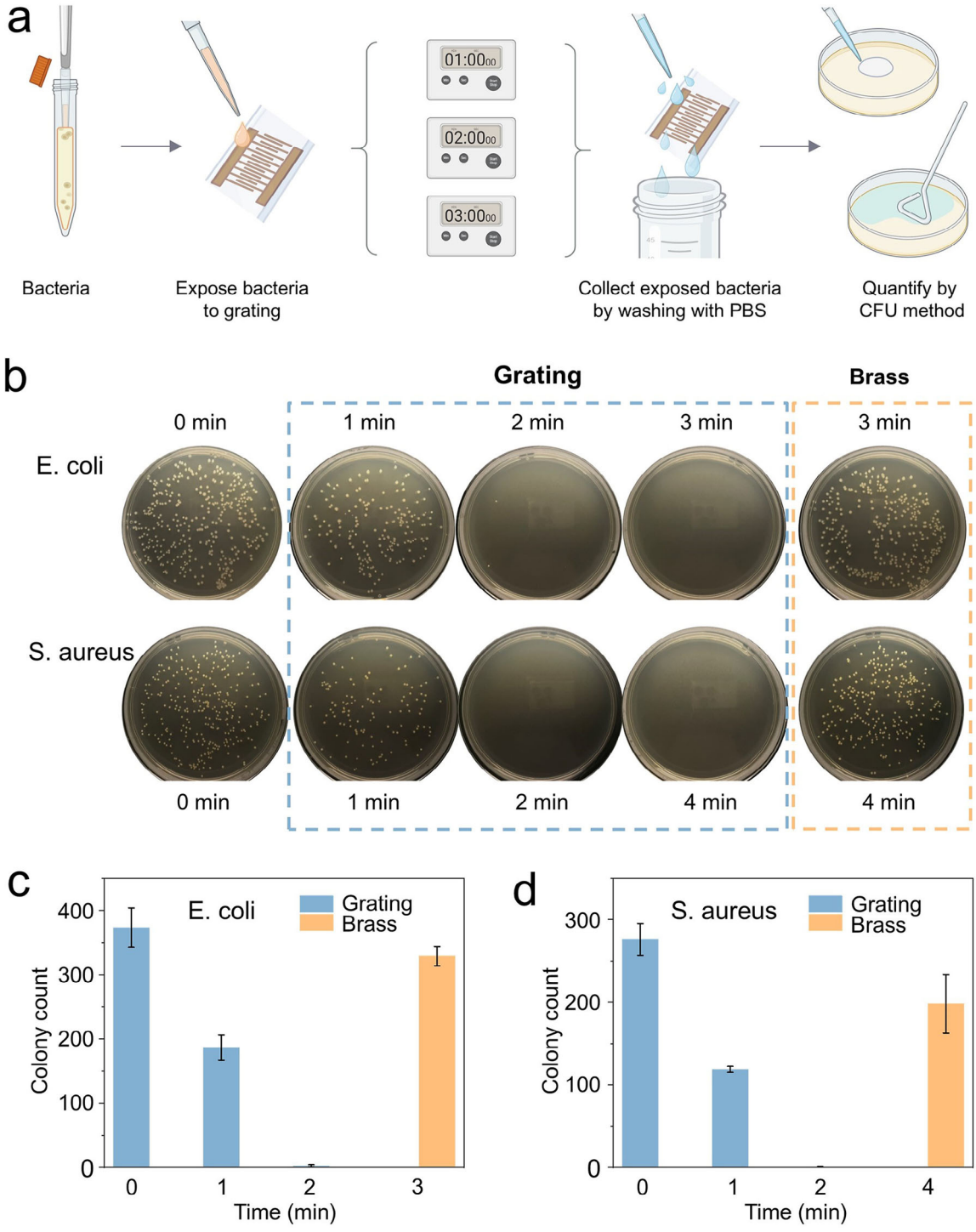

Figure 5. a) Antibacterial experiment workflow; b) optical images of agar plates after incubation for S. aureus and E. coli after sterilization by the Cu/CuZn-ZnO grating and Brass with various contact times; the colony count after contact with Cu/CuZn-ZnO grating and Brass with various durations for c) E.coli and d) S. aureus.

subsequently exploited for droplet detection applications. The inherent superhydrophilicity of the grating facilitates the rapid spread and magnification of minute airborne droplets. Moreover, upon droplet contact, the bridging of adjacent grating lines by the liquid leads to a measurable reduction in electrical resistance, enabling rapid droplet detection. Furthermore, distinct diffraction patterns are discernible between areas of the grating in contact with droplets and those that remain dry. Analysis of these diffraction patterns allows for the rapid and precise localization of droplet deposition on the grating surface. Importantly, the

fabricated grating demonstrates excellent antibacterial efficacy, suggesting significant potential for applications in public health and hygiene. This combination of rapid droplet detection, localization, and antibacterial properties positions the fabricated grating as a promising platform for various sensing and hygiene-related applications.

4. Experimental Section

Fabrication of the Droplet Sensor: The grating structure was achieved using a 1064 nm laser and involved a two-step process. The first step utilized LIBT to transfer the CuZn alloy from a CuZn sheet (donor) onto a glass substrate (acceptor). LIBT parameters were set at a scanning speed of 900 mm/s, 50% laser power, and a line spacing of 0.025 mm. The second step employed LDW to selectively ablate excess CuZn from the glass substrate, leaving the desired micro-grid pattern. This ablation process was performed at a scanning speed of 1500 mms^{-1} and 9% laser power.

Characterization: Optical microscopy images were collected by Leica DM4 M. Contact angle measurement was performed with the Biolin Theta contact angle meter. XRD patterns were acquired by PANalytical X'pert Pro. SEM images were captured with the JEOL-6700F. TEM images were collected using Titan Themis3 G2 300 equipment.

Electrical Measurement: The grating sensor was connected to a 2450 instrument for real-time resistance monitoring. A 0.1 µL droplet of either water or PBS was dispensed onto the electrode, and subsequent droplets were only added after the previous droplet had completely evaporated. For the speaking, coughing, and sneezing experiments, the distance between the subject and the electrode was kept at approximately 10 cm.

Optical Measurement: For optical measurement, a galvo mirror system was employed to direct the laser beam, enabling scanning across a specific region of the grating sensor. Initially, the pristine grating sensor surface was scanned. Subsequently, a 0.5 µL water droplet was dispensed onto the grating sensor, and the same region was rescanned. Laser scanning of the grating sensor in the presence of water revealed a distinct alteration in the diffraction pattern, facilitating the precise localization of the water droplet on the grating sensor surface.

Bacteria Test: The antibacterial efficacy of grating and brass sheet was evaluated against two common bacterial strains: E. coli and S. aureus. For the E. coli sterilization experiments, a 5 µL aliquot of bacterial suspension was deposited onto each brass sheet and allowed to remain in contact for 3 min. Subsequently, the brass sheet was immersed in 10 mL of PBS, and the bacterial droplets were thoroughly mixed into the solution using a vortex mixer. The same procedure was performed for the grating, with the bacterial suspension contact times varied at 1, 2, and 3 min. To ensure robust control measurements, a 5 µL aliquot of bacterial suspension was directly added to 10 mL of PBS and mixed thoroughly. Following each mixing procedure, a 5 µL aliquot of the resultant suspension was diluted with 995 µL of PBS. A 100 µL aliquot of this diluted suspension was then plated onto Petri dishes and incubated at 37 °C for 18 h to allow for colony formation and enumeration. The S. aureus sterilization experiments followed the same protocol as described above, with one modification: the sterilization time of 3 min was replaced with a duration of 4 min.

Supporting Information

Supporting Information is available from the Wiley Online Library or from the author.

Acknowledgements

Y.P. and X.L. contributed equally to this work. The work described in this paper was mainly supported by the funding of the Hong Kong Research Grants Council (25201620, C6001-22Y, and JLFS/P-603/24) and the Hong Kong Innovation and Technology Commission (ITC) under project No. MHP/060/21. The authors would also like to express their sincere thanks to the support from the State Key Laboratory of Advanced Displays and Optoelectronics Technologies at HKUST.

Conflict of Interest

The authors declare no conflicts of interest.

Data Availability Statement

The data that support the findings of this study are available from the corresponding author upon reasonable request.

Keywords

COVID-19, droplet sensing, laser-induced transfer, laser manufacturing, respiratory droplets

Received: April 6, 2025
Published online: May 27, 2025

[1] Coronavirus Disease (COVID-19) Situation Reports (COVID-19 epidemiological update – 9 October 2024), Technical report, World Health Organization, **2024**.
[2] L. Morawska, J. Cao, *Environ. Int.* **2020**, *139*, 105730.
[3] M. A. Shereen, S. Khan, A. Kazmi, N. Bashir, R. Siddique, *J. Adv. Res.* **2020**, *24*, 91.
[4] N. H. L. Leung, D. K. W. Chu, E. Y. C. Shiu, K.-H. Chan, J. J. McDevitt, B. J. P. Hau, H.-L. Yen, Y. Li, D. K. M. Ip, J. S. M. Peiris, W.-H. Seto, G. M. Leung, D. K. Milton, B. J. Cowling, *Nat. Med.* **2020**, *26*, 676.
[5] H. Huang, H. Park, Y. Liu, J. Huang, *Matter* **2020**, *3*, 1791.
[6] N. El-Atab, N. Qaiser, H. Badghaish, S. F. Shaikh, M. M. Hussain, *ACS Nano* **2020**, *14*, 7659.
[7] S. Kim, P. Akarapipad, B. T. Nguyen, L. E. Breshears, K. Sosnowski, J. Baker, J. L. Uhrlaub, J. Nikolich-Žugich, J.-Y. Yoon, *Biosens. Bioelectron.* **2022**, *200*, 113912.
[8] Z. Y. Han, W. G. Weng, Q. Y. Huang, *J. R. Soc., Interface* **2013**, *10*, 20130560.
[9] L. Bourouiba, E. Dehandschoewercker, J. W. M. Bush, *J. Fluid Mech.* **2014**, *745*, 537.
[10] N. van Doremalen, T. Bushmaker, D. H. Morris, M. G. Holbrook, A. Gamble, B. N. Williamson, A. Tamin, J. L. Harcourt, N. J. Thornburg, S. I. Gerber, J. O. Lloyd-Smith, E. de Wit, V. J. Munster, *N. Engl. J. Med.* **2020**, *382*, 1564.
[11] G. Kampf, D. Todt, S. Pfaender, E. Steinmann, *J. Hosp. Infect.* **2020**, *104*, 246.
[12] E. Klement, D. F. Talkington, O. Wasserzug, R. Kayouf, N. Davidovitch, R. Dumke, Y. Bar-Zeev, M. Ron, J. Boxman, W. L. Thacker, D. Wolf, T. Lazarovich, Y. Shemer-Avni, D. Glikman, E. Jacobs, I. Grotto, C. Block, R. Nir-Paz, *Clin. Infect. Dis.* **2006**, *43*, 1239.
[13] J. Tang, Y. Li, I. Eames, P. Chan, G. Ridgway, *J. Hosp. Infect.* **2006**, *64*, 100.
[14] T. Ai, Z. Yang, H. Hou, C. Zhan, C. Chen, W. Lv, Q. Tao, Z. Sun, L. Xia, *Radiology* **2020**, *296*, E32.
[15] M. Yüce, E. Filiztekin, K. G. Özkaya, *Biosens. Bioelectron.* **2021**, *172*, 112752.
[16] M. Adeel, Y. Cotur, A. Naik, L. Gonzalez-Macia, F. Güder, *Nat. Electron.* **2022**, *5*, 719.

[17] H. Zhong, Z. Zhu, J. Lin, C. F. Cheung, V. L. Lu, F. Yan, C.-Y. Chan, G. Li, *ACS Nano* **2020**, *14*, 6213.
[18] J. Zhong, Z. Li, M. Takakuwa, D. Inoue, D. Hashizume, Z. Jiang, Y. Shi, L. Ou, M. O. G. Nayeem, S. Umezu, K. Fukuda, T. Someya, *Adv. Mater.* **2022**, *34*, 2107758.
[19] Y. Fang, J. Xu, X. Xiao, Y. Zou, X. Zhao, Y. Zhou, J. Chen, *Adv. Mater.* **2022**, *34*, 2200252.
[20] J. Ahn, Z.-J. Zhao, J. Choi, Y. Jeong, S. Hwang, J. Ko, J. Gu, S. Jeon, J. Park, M. Kang, D. V. Del Orbe, I. Cho, H. Kang, M. Bok, J.-H. Jeong, I. Park, *Nano Energy* **2021**, *85*, 105978.
[21] Y. Liang, Q. Ding, H. Wang, Z. Wu, J. Li, Z. Li, K. Tao, X. Gui, J. Wu, *Nano-Micro Lett.* **2022**, *14*, 183.
[22] B. Wang, D. Yang, Z. Chang, R. Zhang, J. Dai, Y. Fang, *Matter* **2022**, *5*, 4347.
[23] C. S. H. Hwang, S. Lee, S. Lee, H. Kim, T. Kang, D. Lee, K.-H. Jeong, *ACS Appl. Mater. Interfaces* **2022**, *14*, 54550.
[24] P. Escobedo, M. D. Fernández-Ramos, N. López-Ruiz, O. Moyano-Rodríguez, A. Martínez-Olmos, I. M. Pérez De Vargas-Sansalvador, M. A. Carvajal, L. F. Capitán-Vallvey, A. J. Palma, *Nat. Commun.* **2022**, *13*, 72.
[25] L. Pan, C. Wang, H. Jin, J. Li, L. Yang, Y. Zheng, Y. Wen, B. H. Tan, X. J. Loh, X. Chen, *ACS Mater. Lett.* **2020**, *2*, 1178.
[26] S. Fikenzer, T. Uhe, D. Lavall, U. Rudolph, R. Falz, M. Busse, P. Hepp, U. Laufs, *Clin. Res. Cardiol.* **2020**, *109*, 1522.
[27] J. L. Scheid, S. P. Lupien, G. S. Ford, S. L. West, *Int. J. Environ. Res. Public Health* **2020**, *17*, 6655.
[28] S. Faridi, S. Niazi, K. Sadeghi, K. Naddafi, J. Yavarian, M. Shamsipour, N. Z. S. Jandaghi, K. Sadeghniiat, R. Nabizadeh, M. Yunesian, F. Momeniha, A. Mokamel, M. S. Hassanvand, T. MokhtariAzad, *Sci. Total Environ.* **2020**, *725*, 138401.
[29] J. V. Puthussery, D. P. Ghumra, K. R. McBrearty, B. M. Doherty, B. J. Sumlin, A. Sarabandi, A. G. Mandal, N. J. Shetty, W. D. Gardiner, J. P. Magrecki, D. L. Brody, T. J. Esparza, T. L. Bricker, A. C. M. Boon, C. M. Yuede, J. R. Cirrito, R. K. Chakrabarty, *Nat. Commun.* **2023**, *14*, 3692.
[30] H. Xiong, X. Ye, Y. Li, J. Qi, X. Fang, J. Kong, *Anal. Chem.* **2021**, *93*, 4270.
[31] P. Anfinrud, V. Stadnytskyi, E. B. Christina, B. Adriaan, *N. Engl. J. Med.* **2020**, *382*, 2061.
[32] G. A. Somsen, C. J. M. van Rijn, S. Kooij, R. A. Bem, D. Bonn, *Phys. Fluids* **2020**, *32*, 121707.
[33] J. Lai, B. Sunderland, J. Xue, S. Yan, W. Zhao, M. Folkard, B. D. Michael, Y. Wang, *Appl. Surf. Sci.* **2006**, *252*, 3375.
[34] W. Chen, L. Nichols, F. Brinkley, K. Bohna, W. Tian, M. W. Priddy, L. B. Priddy, *Mater. Sci. Eng., C* **2021**, *120*, 111686.
[35] Z. Xu, L. Li, J. Liu, C. Dai, W. Sun, J. Chen, Z. Zhu, M. Zhao, H. Zeng, *J. Colloid Interface Sci.* **2022**, *608*, 702.
[36] Z. Wu, D. Sun, C. Shi, S. Chen, S. Tang, Y. Li, C. Yan, Y. Shi, B. Su, *Adv. Funct. Mater.* **2023**, *33*, 2304897.
[37] H. Liu, Y. Zheng, K.-S. Moon, Y. Chen, D. Shi, X. Chen, C.-P. Wong, *Nano Energy* **2022**, *94*, 106902.
[38] Y. He, K. Yin, L. Wang, T. Wu, Q. Deng, Y. Dou, C. J. Arnusch, *Nano Lett.* **2023**, *23*, 4947.
[39] J. Lu, X. Chen, X. Ding, Z. Jia, M. Li, M. Zhang, F. Liu, K. Tang, X. Yu, G. Li, *Adv. Sci.* **2024**, *11*, 2401940.
[40] J. Liu, W. Zhao, J. Li, C. Li, S. Xu, Y. Sun, Z. Ma, H. Zhao, L. Ren, *Biosens. Bioelectron.* **2024**, *243*, 115773.
[41] A. Roth, D. Frantz, M. Stiti, E. Berrocal, *J. Aerosol Sci.* **2023**, *174*, 106257.
[42] Y. Xu, J. Lin, Y. Chen, H. Zhong, C. K. W. Lee, M. Tan, S. Chen, M. Kim, E. W. Y. Poon, T. Y. H. Chan, A. Q. Yuan, M. Tang, R. Yang, Y. Pan, Y. Fu, M. G. Li, *Adv. Mater. Interfaces* **2024**, *11*, 2400045.
[43] M. L. Ermini, V. Voliani, *ACS Nano* **2021**, *15*, 6008.
[44] R. Shahvalizadeh, R. Ahmadi, I. Davandeh, A. Pezeshki, S. A. Seyed Moslemi, S. Karimi, M. Rahimi, H. Hamishehkar, M. Mohammadi, *Food Chem.* **2021**, *354*, 129492.
[45] N. Y. Elmehbad, N. A. Mohamed, N. A. Abd El-Ghany, M. M. Abdel-Aziz, *Int. J. Biol. Macromol.* **2023**, *246*, 125582.
[46] J. Zi, X. Yu, Y. Li, X. Hu, C. Xu, X. Wang, X. Liu, R. Fu, *Proc. Natl. Acad. Sci. USA* **2003**, *100*, 12576.
[47] A. K. Chatterjee, R. Chakraborty, T. Basu, *Nanotechnology* **2014**, *25*, 135101.
[48] M. Shi, H. S. Kwon, Z. Peng, A. Elder, H. Yang, *ACS Nano* **2012**, *6*, 2157.
[49] N. Babayevska, L. Przysiecka, I. Iatsunskyi, G. Nowaczyk, M. Jarek, E. Janiszewska, S. Jurga, *Sci. Rep.* **2022**, *12*, 8148.
[50] Q. Yu, X. Xu, C. Wang, Y. Ma, D. Hui, Z. Zhou, *Composites, Part B* **2017**, *110*, 32.